

# Multi-filter photometry of Solar System Objects from the SkyMapper Southern Survey <sup>★</sup>

A. V. Sergeev<sup>1,7</sup>, B. Carry<sup>1</sup>, C. A. Onken<sup>2,3</sup>, H. A. R. Devillepoix<sup>4</sup>, C. Wolf<sup>2,3</sup>, and S.-W. Chang<sup>2,5,6</sup>

<sup>1</sup> Université Côte d'Azur, Observatoire de la Côte d'Azur, CNRS, Laboratoire Lagrange, France  
e-mail: alexey.sergeyev@oca.eu; benoit.carry@oca.eu

<sup>2</sup> Research School of Astronomy and Astrophysics, Australian National University, Canberra, ACT 2611, Australia

<sup>3</sup> Centre for Gravitational Astrophysics, College of Science, The Australian National University, ACT 2601, Australia

<sup>4</sup> School of Earth and Planetary Sciences, Curtin University, Perth WA 6845, Australia

<sup>5</sup> SNU Astronomy Research Center, Seoul National University, 1 Gwanak-rho, Gwanak-gu, Seoul 08826, Korea

<sup>6</sup> Astronomy program, Dept. of Physics & Astronomy, SNU, 1 Gwanak-rho, Gwanak-gu, Seoul 08826, Korea

<sup>7</sup> V. N. Karazin Kharkiv National University, 4 Svobody Sq., Kharkiv, 61022, Ukraine

.../...

## ABSTRACT

*Context.* The populations of small bodies of the Solar System (asteroids, comets, Kuiper Belt objects) are used to constrain the origin and evolution of the Solar System. Both their orbital distribution and composition distribution are required to track the dynamical pathway from their regions of formation to their current locations.

*Aims.* We aim at increasing the sample of Solar System objects (SSOs) that have multi-filter photometry and compositional taxonomy.

*Methods.* We search for moving objects in the SkyMapper Southern Survey. We use the predicted SSO positions to extract photometry and astrometry from the SkyMapper frames. We then apply a suite of filters to clean the catalog for false-positive detections. We finally use the near-simultaneous photometry to assign a taxonomic class to objects.

*Results.* We release a catalog of 880,528 individual observations, consisting of 205,515 known and unique SSOs. The catalog completeness is estimated to be about 97% down to  $V=18$  mag and the purity to be above 95% for known SSOs. The near-simultaneous photometry provides either three, two, or a single color that we use to classify 117,356 SSOs with a scheme consistent with the widely used Bus-DeMeo taxonomy.

*Conclusions.* The present catalog contributes significantly to the sample of asteroids with known surface properties (about 40% of main-belt asteroids down to an absolute magnitude of 16). We will release more observations of SSOs with future SkyMapper data releases.

**Key words.** Catalogs; Minor planets, asteroids: general

## 1. Introduction

The small bodies of our Solar System (asteroids, comets, Kuiper-belt objects) are the remnants of the building blocks that accreted to form the planets. Their orbital and compositional distributions hold the record of the events that shaped our planetary system (Levison et al. 2009; DeMeo & Carry 2014; Morbidelli et al. 2015; Clement et al. 2020).

While the number of known Solar System Objects (hereafter SSOs) has increased to over a million, the fraction of SSOs with known composition remains limited. Spectroscopy in the visible and near-infrared have been used for decades to assert the composition, but the sample remains small (several thousands, e.g., Bus & Binzel 2002; DeMeo et al. 2009; Fornasier et al. 2014; Devogèle et al. 2019; Binzel et al. 2019). On the other hand, multi-filter photometry can be used to classify SSOs in broad compositional groups, providing less details but on large samples (up to several hundreds of thousands, e.g., Ivezić et al. 2001; Popescu et al. 2016; Sergeev & Carry 2021)

We analyze here the images from the SkyMapper Southern Survey (Minor Planet Centre (MPC) observatory code *Q55*), which uses a suite of filters well-adapted to asteroid spectral characterization (Figure 1), similar to those of the Sloan Digital Sky Survey (SDSS, the main source of compositional information over almost two decades; Szabó et al. 2004; Nesvorný et al. 2005; Carvano et al. 2010; DeMeo & Carry 2013; DeMeo et al. 2014; DeMeo et al. 2019; Parker et al. 2008; Graves et al. 2018). While the SDSS finished its imaging survey in 2009, SkyMapper has started its operations in 2014 and is currently active.

The present article aims to increase the number of asteroids with multi-filter photometry and taxonomy by identifying known SSOs in the SkyMapper source catalog. The article is organized as follows. In Section 2, we summarize the characteristics of the SkyMapper Southern Survey. In Section 3, we describe how we extract SSOs observations from the SkyMapper point-source catalog, and detail the filters applied to the sample to reject false-positive sources in Section 4. The completeness and purity of the catalogue is estimated in Section 5. We present the catalog of SSO colors in Section 6, and use it to classify the SSOs consistently with the DeMeo et al. (2009) taxonomic classification in Section 7. We present our plan for future releases in Section 8. Finally, we summarize the released asteroid sample in Section 9.

<sup>★</sup> The catalogs presented here are available at the CDS via anonymous ftp to <http://cdsarc.u-strasbg.fr/> or via <http://cdsarc.u-strasbg.fr/viz-bin/qcat?J/A+A/xxx/Axxx>

## 2. The SkyMapper survey

The SkyMapper Southern Survey (SMSS) is producing a homogeneous multi-band atlas of the whole Southern Hemisphere in  $u, v, g, r, i, z$  filters (Wolf et al. 2018). Observations were carried out with a 1.35m telescope located at Siding Spring Observatory (IAU code Q55). The telescope has an f/4.8 focal ratio and is equipped with a mosaic CCD camera having 268 million pixels. The third data release (DR3) covers an area of more than 24,000 deg<sup>2</sup> and contains over 200,000 images with over 8 billion individual source detections (see the SkyMapper website<sup>1</sup> and the DR2 release article for details: Onken et al. 2019). The data in DR3 were obtained between March 2014 and October 2019. Individual deep exposures can reach magnitudes of 20 in  $u, v, z$ , 21 in  $i$ , and 22 in  $g, r$  ( $10\sigma$  detections) in the AB system (Oke & Gunn 1983). The median seeing ranges from 3.3'' in  $u$  to 2.5'' in  $z$ .

The SMSS covers each field on the sky in three primary modes: a shallow 6-filter sequence with exposure times between 5 and 40 seconds that reaches depths of 18 ABmag, a deep 10-image sequence of  $uvgrvizuv$  with 100-second exposures, and pairs of deep exposures in  $gr$  and  $iz$ . This observing strategy, in conjunction with the enhanced sensitivity of  $g, r$ , gives rise to a predominance of  $g - r$  colors in the results presented in Section 6, but almost always leads to the measurement of at least one photometric color obtained with  $\leq 2$  minutes between exposure midpoints in the two filters.

The work presented here adopts a single photometric measurement associated with each SkyMapper image, although for objects with significant motion during the exposure, additional information on shape and rotation parameters may be available from a more detailed analysis (e.g., the SkyMapper observations of the Earth-impacting 2018 LA, Jenniskens et al. 2021). We present a typical suite of images illustrating the apparent motion of SSOs in SkyMapper frames (Figure 2).

## 3. Extracting candidate SSOs

For each of the 208,860 images contained in SMSS DR3, we compile all known SSOs potentially present in the images by performing a search with SkyBoT (Berthier et al. 2006, 2016), a Virtual Observatory Web Service providing a cone-search utility for Solar System objects. The 2° cone-search radius utilised is slightly larger than the 1.7° centre-to-corner size of the SkyMapper camera and returned 43,501,635 predicted SSOs locations with no initial filtering with a magnitude limit. Among these, 16,915,791 are predicted within the field of view. The smaller number in the number of SSO predicted locations is explained by the search and FoV area difference.

For each predicted SSO position, we extract all sources listed in the SMSS DR3 photometry table<sup>2</sup> within a radius of twice the SkyBoT-reported position uncertainty (with a floor of 5''). We obtain a list of 9,367,950 SkyMapper sources, associated with the 2,047,588 predicted SSO positions.

## 4. Rejecting false-positive sources

The fraction of interlopers among the 9,367,950 sources extracted above is large. First, multiple SkyMapper sources may be located by mere chance in close vicinity to predicted SSO

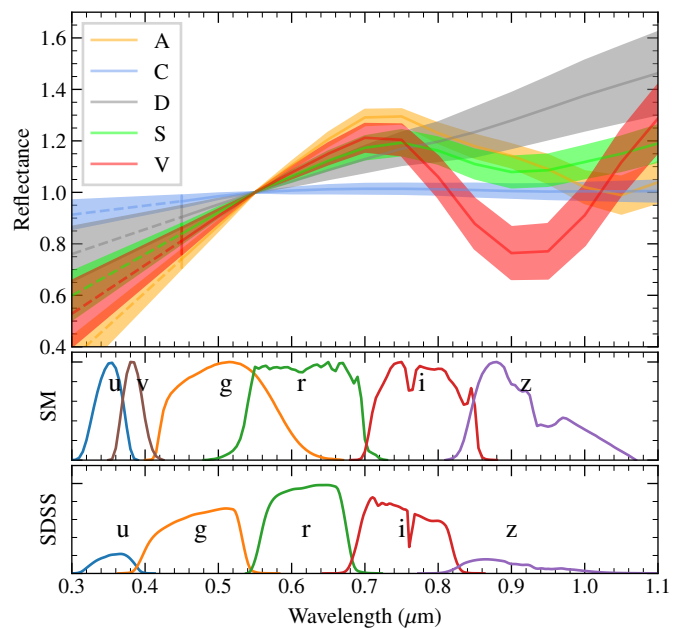


**Fig. 1.** Reflectance spectra of A, C, D, S, and V asteroid classes from DeMeo et al. (2009) normalized at 550nm. SkyMapper filters (transmission curves for a normalized quantum efficiency of the CCD are shown in SM panel) are well-adapted to spectral characterization. We also report SDSS filters for comparison.

positions. Second, many SSOs are too faint to have been imaged by SkyMapper, and the extracted sources correspond to spurious associations. We thus apply two filters to the extracted sources to reject false-positive SSOs associations.

### 4.1. Comparison with Gaia

We first identify stationary sources (stars, unresolved galaxies) by comparing the catalog of sources with Gaia DR2 (Brown et al. 2018). We find 8,203,916 Gaia sources within 2'' (less than the median SkyMapper seeing, Section 2) of the extracted sources. Although this certainly includes some real associations with observed SSOs, we remove them from the catalog to avoid introducing biases in the measured photometry.

### 4.2. Comparison with the expected photometry

We present in Figure 3 a comparison of the predicted V magnitudes of SSOs with SkyMapper-measured magnitudes. These magnitudes are in almost all cases the PSF (Point Spread Function) photometry. However, owing to the apparent motion of SSOs during an exposure, the PSF photometry may underestimate the true magnitude of the observed SSO. We computed this underestimation as a function of exposure time and SSO apparent velocity. We report PSF magnitudes for most SSO observations, only reporting Petrosian magnitudes for observed SSOs with an apparent velocity of more than 50''/hour and image exposure time of 100 s. PSF photometry was preferred over Petrosian overall due to its higher accuracy in the case of non-trailed sources.

Many contaminants are still present, and easily identified by their large magnitude difference with respect to the predicted magnitudes. These contaminants correspond to SSOs too faint to have been detected, and erroneously associated to stationary sources.

<sup>1</sup> See <https://skymapper.anu.edu.au>

<sup>2</sup> The SMSS photometry table contains the per-image measurements, as opposed to the averaged quantities in the master table.

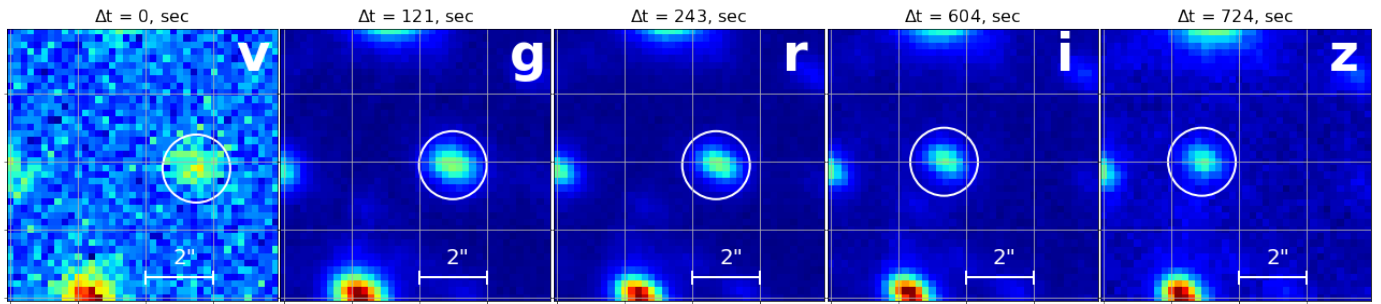


**Fig. 2.** SkyMapper multi-color observations of SSOs, here the asteroid (4365) Ivanova. The time interval between each frame and the first one (here  $v$ ) is reported above each image. North is up and East is left.

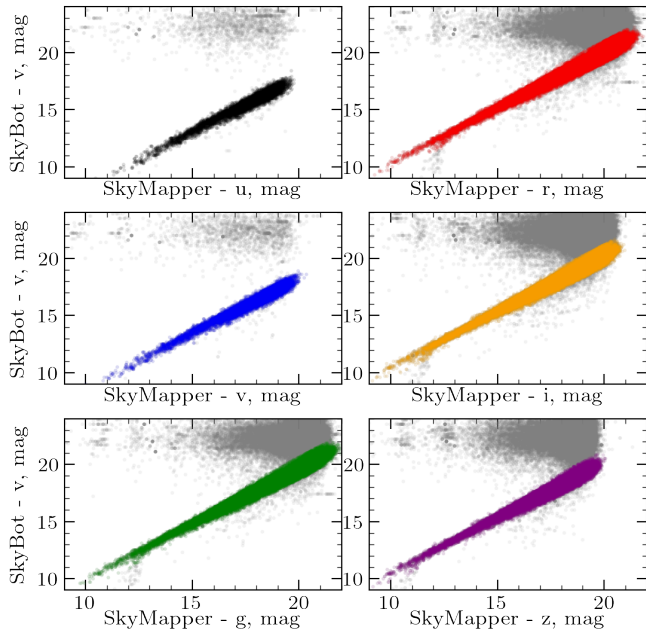


**Fig. 3.** Measured SkyMapper magnitude in each filter compared with the predicted  $V$  magnitude of SSOs (colored dots). The light grey dots correspond to rejected sources, spuriously associated to SSOs too faint to have been detected (see text).

As these contaminants tend to be located at large angular separation from the predicted SSO position, we reject all sources farther than  $5''$  from SkyBoT prediction (which also implies a high SkyBoT position uncertainty). The next cleaning procedure was based on the SkyBoT and SkyMapper magnitude difference. We compared visual magnitudes as predicted by SkyBoT with the SkyMapper sample and calculated regression slopes and offsets for each filter, which are presented in the Table 1. Then we removed sources showing a difference in magnitude minus the photometry magnitude error larger than 1.0 mag. A few observed SSOs appear to have saturated ( $g, r, i$  filters), with magnitudes  $\lesssim 10$  in shallow images or  $\lesssim 13.8, 13.8, 13$  in deeper images, and the latter condition removes them too.

Finally, whenever several SkyMapper sources remain associated with a SSO, we select the closest and reject the others. After these steps of filtering, we obtained a list of 880,528 measurements of 205,515 individual SSOs. We present their distribution on sky in Figure 4.

The mean difference between predicted and measured SSO positions are  $-0.014$  and  $-0.075$  arcsec with standard deviations of 0.15 and 0.11 arcsec for RA and DEC respectively (Figure 5),

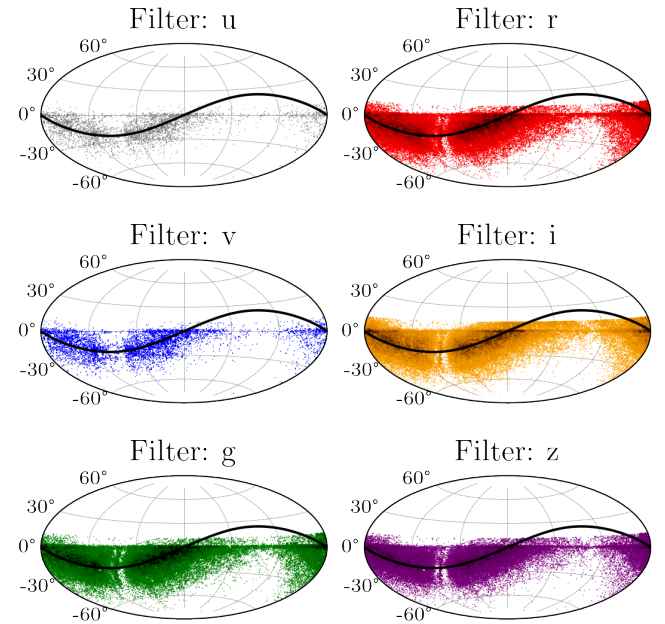


**Fig. 4.** Sky distribution (equatorial frame) of 880,528 SkyMapper SSO observations in each filter. The black curve represents the ecliptic plane.

Filter	Slope	Offset	#SSOs
u	0.927	-0.776	2850
v	0.937	-0.550	5302
g	0.976	0.133	129789
r	0.973	0.571	151809
i	0.971	0.814	125395
z	0.968	0.837	62774

**Table 1.** Average values of the slope and the magnitude offset between SkyBoT SSOs visual magnitude and each SkyMapper band magnitude.

well below the typical seeing of SkyMapper images. Though the mean number of observations for an individual SSO is about four, hundreds of asteroids have dozens of observations, while most of them were observed only one or two times see Figure 6. We present the distribution of measurements among dynamical classes in Table 2, and describe the catalog of measurements in Appendix A.

## 5. Purity and completeness

The completeness indicates the fraction of reported SSO observations with respect to how many SSOs were present in the

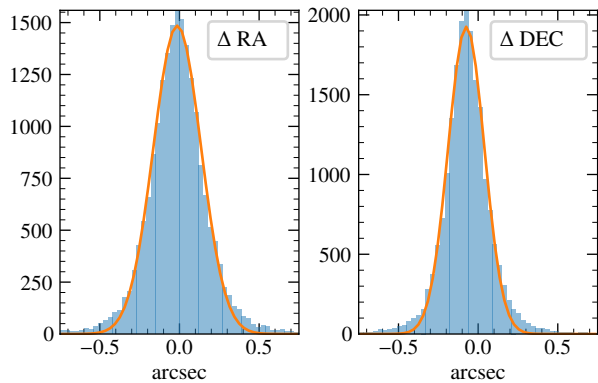


**Fig. 5.** The distribution of the coordinate difference between SkyMapper sources and predicted by SkyBoT SSO positions.

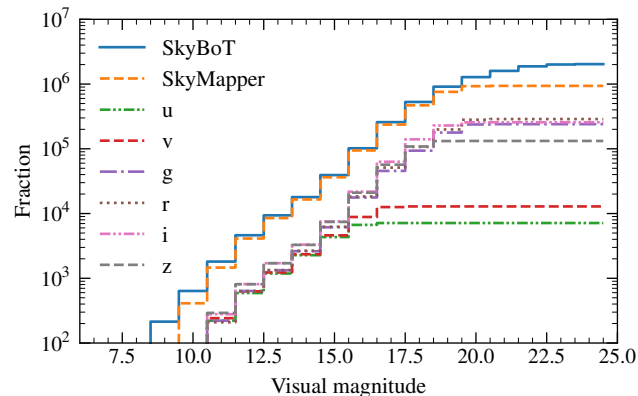


**Fig. 7.** Completeness as function of predicted V magnitude for the whole catalog (SkyMapper), and for each filter.

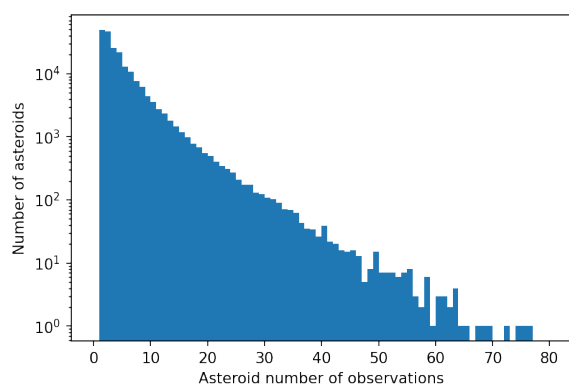


**Fig. 6.** The SkyMapper distribution of asteroid observations.

**Table 2.** Number of observations ( $N_{\text{obs}}$ ) of  $N_{\text{obj}}$  unique objects, sorted by dynamical classes. NEA, MBA, and KBO stand for Near-Earth Asteroid, Main-belt Asteroid, and Kuiper Belt Object.

Dynamical class	$N_{\text{obj}}$	$N_{\text{obs}}$
NEA>Aten	39	103
NEA>Apollo	282	822
NEA>Amor	348	1289
Mars-Crosser	2,487	9,807
Hungaria	4,035	13,803
MBA>Inner	65,231	287,664
MBA>Middle	71,677	301,935
MBA>Outer	57,721	245,664
MBA>Cybele	811	4,481
MBA>Hilda	829	4,298
Trojan	1,928	10,103
Centaur	24	127
KBO	37	189
Comet	65	226
Planet	1	17
Total	205,515	880,528

field of view. The purity indicates the fraction of contamination among the released observations. For both estimators, the closer to unity the better. We estimate the completeness by comparing the number of SSO observations predicted by SkyBoT with the number of sources after filtering.

**Table 3.** Purity (expressed in percent) of MBAs, NEAs, and KBOs, as function of their apparent V magnitude. We also the number of sources ( $N$ ) we visually check in each magnitude bin.

V (mag)	$N_{\text{MBA}}$	$N_{\text{NEA}}$	$N_{\text{KBO}}$	MBA (%)	NEA (%)	KBO (%)
10	0	0	0	-	-	-
11	2	5	0	100	100	-
12	2	0	0	100	-	-
13	4	23	0	100	100	-
14	6	5	0	100	100	-
15	14	23	49	100	100	100
16	40	83	0	100	99	-
17	105	247	0	100	100	-
18	174	321	14	100	100	100
19	289	421	29	100	100	100
20	298	418	54	99	99	100
21	63	133	30	94	93	97
22	2	4	4	50	100	75
23	0	0	0	-	-	-

At face value (16,915,791 vs 880,528), the completeness is 5% only. Most non-detected SSOs are, however, simply those beyond the SkyMapper field of view, or too faint to be detected. Thus the completeness of the sources inside the CCD field of view for V between 11 and 18 mag is above 97%. (Figure 7)

We estimated the purity through a visual inspection of frames centered on SSO positions in both SkyMapper and Pan-STARRS (Panoramic Survey Telescope And Rapid Response System) archives. We generated cut-out frames using the SkyMapper image cutout service<sup>3</sup>, and downloaded Pan-STARRS cut-out stacked images at the same coordinates (Chambers et al. 2016). The Pan-STARRS survey has a significantly deeper limiting magnitude. Thus, all stationary SkyMapper sources should hence be visible in Pan-STARRS images. As the Pan-STARRS survey did not image the sky below  $-30^\circ$  of declination, we test the purity for sources located North of this declination only.

We inspected all available 189 KBOs (Kuiper Belt Objects) observations, 1,683 NEAs (Near Earth Asteroids), and 1,000 randomly selected MBAs (Main Belt Asteroids) observations with declination of greater than  $-30^\circ$ . The purity of the SkyMapper SSOs survey is about 100% down to magnitude  $V \approx 20$ , where it begins to drop (Table 3).

<sup>3</sup> See <https://skymapper.anu.edu.au/how-to-access/>

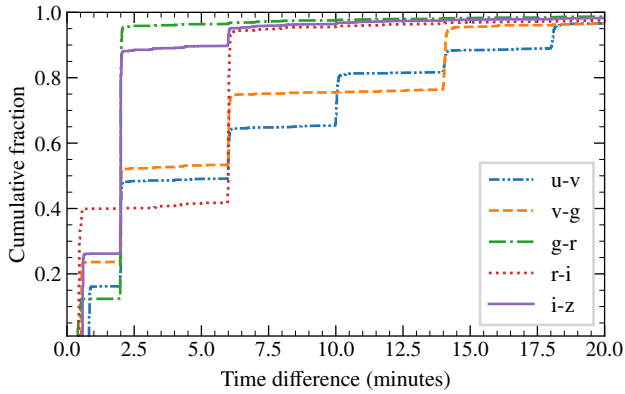


Fig. 8. Cumulative histogram of the time difference between filters.

## 6. Computation of colors

We build the colors of the detected SSOs for compositional (taxonomic) purposes. Due to the intrinsic photometric variability of asteroids caused by their irregular shape (Szabó et al. 2004; Popescu et al. 2016; Carry 2018), color indices have to be calculated from near-simultaneous observations. We only consider observations taken within a maximum of 20 minutes of each other. Although this threshold may appear large, it mainly affects  $u$  and  $v$  filter combinations. The majority (95+%) of  $g-r$  and  $i-z$  colors were acquired within 2 minutes, and  $r-i$  in 6 minutes (Figure 8).

Szabó et al. (2004) analyzed the color variability of asteroids from the 4th SDSS Moving Object Catalog (MOC4), and with conservative assumptions, showed that 5-minute time differences have an effect on the color of less than 0.03 mag. Therefore, the typical 2-minute difference in our  $g-r$  and  $i-z$  data will not have a significant effect on the color estimation.

We provide the catalog of 669,545 measured colors of 139,220 SSOs, specifying the time difference between each acquisition, and describe the catalog elements in Appendix A.

Some asteroids had their colors measured multiple times. We thus calculated the weighted mean colors value of individual SSOs, taking into account the magnitude uncertainty and the time difference between observations and set weights as:  $1/mag_{err} + 0.1/\Delta d$ , where  $\Delta d$  is the time difference in days while  $mag_{err} = \sqrt{mag1_{err}^2 + mag2_{err}^2}$  is color uncertainty of two photometry measurements  $mag1, mag2$ . If the SSO has multiple color measurements the error was computed as the weighted mean value of color uncertainties. We also computed 13,783 colors that were not directly observed, but are combinations of measured colors: for instance, we compute  $r-z$  from  $g-r$  and  $g-z$ .

As a result, we constructed a catalog of 139,220 SSOs which contain at least one measured color. The total number of unique SSO colors is 388,943, both observed and derived (Table 4).

In order to check the time lag effect on the SkyMapper asteroids colors, we estimated the dependence of brightness variability on asteroids rotation period. We downloaded the latest data release from the Asteroid Lightcurve Database<sup>4</sup> which contains periods and amplitudes of more than 30,000 known SSOs. Then we compared SkyMapper data and selected joint asteroids. We obtained samples of more than twelve thousands asteroids with  $g-r$  and  $i-z$  colors and almost eight thousand asteroids with  $g-i$  colors. For each asteroid in the samples, we calculated the maximum expected color change arising from asteroid rotation

Table 4. Number of measured colors ( $N_{mes}$ ) for each pair of filters, associated with  $N_{obj}$  unique SSOs. We also report the number of colors computed from linear combination of colors ( $N_{comp}$ , see text).

Color	$N_{mes}$	$N_{obj}$	$N_{comp}$
$g-r$	201,910	117,356	205
$i-z$	130,065	57,735	186
$r-i$	86,518	58,626	1,425
$g-i$	74,693	54,759	2,737
$r-z$	55,560	36,689	3,383
$g-z$	48,290	34,333	4,066
$u-v$	12,028	2,628	26
$v-g$	9,963	4,316	211
$v-r$	9,813	4,317	245
$v-z$	9,461	4,241	306
$v-i$	9,396	4,254	331
$u-g$	5,620	2,432	139
$u-r$	5,551	2,434	148
$u-z$	5,363	2,410	176
$u-i$	5,314	2,413	199
Total	669,545	388,943	13,783

between the SkyMapper imaging epochs (still limited to a 20-minute window) as the product of the photometric amplitude and the number of half-periods represented by the SkyMapper time difference.

The magnitude difference in our samples from the rotation effect was less than the color uncertainties for 96, 97, and 87 percent of asteroids in  $g-r$ ,  $i-z$ , and  $g-i$  colors, and thus we consider the overall impact of rotation on the colors we report to be small.

## 7. Taxonomy

We used the multi-color photometry to classify asteroids in a scheme consistent with the widely used Bus-DeMeo taxonomy (DeMeo et al. 2009) in which asteroid color values are used to define belonging to a certain taxonomy complex. Following our recent work with the SDSS (Sergeev & Carry 2021), we use a modified version of the approach of DeMeo & Carry (2013) which a decision tree based on colors is used to assign the taxonomic class. Where, for the each asteroid, we calculate the probability of it being associated with each taxonomic broad complex (A, B, C, D, K, L, Q, S, V, and X). We computed the intersection between the volume occupied by each taxonomy complex and the color(s) of the asteroid, represented as a  $n$ -dimensional Gaussian probability density function based on color values and its uncertainties. (Sergeev & Carry 2021).

### 7.1. SkyMapper taxonomy boundaries

We first convert the color ranges of each taxonomic class (DeMeo & Carry 2013) from SDSS to SkyMapper filters. We used the color coefficients of Casagrande et al. (2019) and Huang et al. (2019). We compared the  $g-r$ ,  $g-i$ , and  $i-z$  values from SkyMapper with those from the SDSS for a wide range of stellar classes (Figure 9, data from Pickles (1998)). We fitted the color-color dependency by linear regression using the Siegel (1982) approximation. These linear coefficients were used to convert the SDSS color boundaries into the SkyMapper photometric system.

<sup>4</sup> See <https://minplanobs.org/MPInfo/php/lcdb.php>

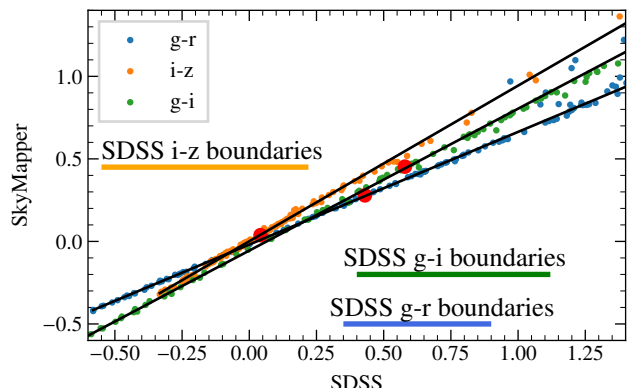


**Fig. 9.** The  $g-r$  (blue),  $g-i$  (green), and  $i-z$  (orange) colors from the SDSS compared with SkyMapper for a wide range of stellar classes. Red dots represent the colors of the Sun (Holmberg et al. 2006). The colored horizontal lines illustrate the range of colors for the SDSS asteroids taxonomy (Sergeyev & Carry 2021).

## 7.2. Multi-color based taxonomy

Owing to the survey strategy, not all SSOs have the same suite of colors (Table 4). We thus adapt our approach (Sergeyev & Carry 2021) to handle both three-color ( $g-r$ ,  $g-i$ ,  $i-z$ ) and two-color ( $g-r, i-z$ ), ( $g-i, i-z$ ), or ( $r-i, i-z$ ) – cases. We restrict the list of pairs of colors to those containing  $i-z$ : it probes the  $1\mu\text{m}$  absorption band which is among the most characteristic spectral feature asteroid taxonomies (Chapman et al. 1975). We also shrink the boundaries to more stringent ranges for the cases with two colors only.

For each observation, we compute the volume it occupies in the color space (either 2D or 3D) based on the corresponding Gaussian distribution, whose  $\sigma$  are set to color uncertainties. We then compute a score for each class,  $\mathcal{P}_k$ , based on the volume of the intersection between the volume of each observation and the space occupied by each taxonomic complex (Figure 10), normalized by the volume of the Gaussian:

$$V_\sigma = \prod_{j=1}^N \left( \text{erf} \left[ \frac{b_j - \mu_j}{\sqrt{2}\sigma_j} \right] - \text{erf} \left[ \frac{a_j - \mu_j}{\sqrt{2}\sigma_j} \right] \right), \quad (1)$$

where  $\text{erf}(z)$  is the error function,  $\text{erf}(z) = \frac{2}{\sqrt{\pi}} \int_0^z e^{-t^2} dt$ , the index  $j$  indicates the colors (with  $N \in \{2, 3\}$ ),  $a_j$  and  $b_j$  are the color boundaries of the complexes, and  $\mu_j$  and  $\sigma_j$  are the color and uncertainty of the SSO. Hence, for a given observation, the volumes of all intersections sum to one. These normalized volumes correspond to the probabilities  $\mathcal{P}_k$  of pertaining to each taxonomic class.

We then assign to each object its most probable class. The only exception to that rule is the unknown class (labeled U), which is assigned only if its probability is strictly equal to 1. Otherwise, whenever U is the most probable but not equal to unity, we assigned the second most-probable class. As an example, we present in Figure 10 the distribution in the three colors space of 29,779 asteroids for which the probability is above 0.2 (out of 32,776 asteroids with three colors). Their pseudo-reflectance spectra in Figure 11 (computed using the solar colors of Holmberg et al. 2006, adapted to SkyMapper) show a good agreement with the template spectra of taxonomic classes (DeMeo et al. 2009).

**Table 5.** Number of asteroids in each taxonomic complex, for different color sets.

Complex	$(gr, gi, iz)$	$(gr, iz)$	$(gi, iz)$	$(ri, iz)$	$(gr)$
A	537	309	947	4,551	
B	1,914	4,587	2,760	1,317	
C	2,180	6,175	2,735	3,554	40,573
D	466	901	1,544	1,404	
K	1,005	1,254	2,661	882	
L	1,709	3,611	1,275	973	
Q	164	633	845	532	
S	8,256	13,753	10,577	10,608	76,783
V	1,787	1,125	843	1,573	
X	4,876	2,398	4,448	5,479	
U	9,882	4,317	4,664	4,625	
Total	32,776	39,063	33,299	35,498	117,356

We illustrate the potential of this taxonomic classification in Figure 12 the photometric classes show clear concentrations in the orbital parameters for different asteroid families. For example asteroids of the Vesta family (light green points) are concentrated in the inner belt which is otherwise dominated by asteroids of S complex (red points). C and B complexes dominate in the outer belt region, however, the Koronis family at 2.9 AU distance shows a clear S complex taxonomy. It is interesting to note that X-type asteroids (indicated by gray points) are a mixture of P, M, and E asteroid types by Tholen classification (Tholen 1989), concentrate in the outer belt region associated with the Eos family.

We test this classification by comparing the SkyMapper classes against previously reported taxonomy from spectroscopy (e.g., Bus & Binzel 2002; Lazzaro et al. 2004; Binzel et al. 2019; Fornasier et al. 2004, 2014). We found 1,683 common SSOs and compare their classes in Figure 13). As expected, rare and peculiar classes such as A, K, L and Q may be underestimated here, and misclassified as S. Similarly, there is some confusion between C/B and C/X classes, that only differ by spectral slope. The values are, however, concentrated on the diagonal of the confusion matrix, showing an overall agreement.

We repeat the same exercise for each SSO with two colors among ( $g-r, i-z$ ), ( $g-i, i-z$ ), or ( $r-i, i-z$ ), accounting for 39,063, 33,299, and 35,498 SSOs, respectively. We present the statistic for all these taxonomic classes in Table 5.

## 7.3. Single-color based taxonomy

A large number of 117,356 SSOs in SkyMapper have only one color:  $g-r$ . A detailed classification cannot be achieved, but this color can still be used to split asteroids into mafic-silicate rich and opaque-rich. Similarly to the work by (Erasmus et al. 2020), we thus classed the asteroids into S-like and C-like objects (hereafter labeled  $S_1$  and  $C_1$ ). The  $g-r$  colors of asteroids clearly present a bi-modal distribution, well-represented by two normal distributions (Figure 14) corresponding to the  $C_1$  (bluer) and  $S_1$  (redder) classes.

From these two normal distributions, we assign a probability of belonging to each complex to each asteroid. We then assign to each objects its most probable complex. Such way we classified 71,822 asteroids as a  $S_1$  type and 40,590 as  $C_1$  type, with the exception of the 4,944 asteroids which probability did not differ by more than 10%. The distribution of  $S_1$  and  $C_1$  asteroids also reproduce the known distribution of compositions in the asteroids belt (Figure 15).

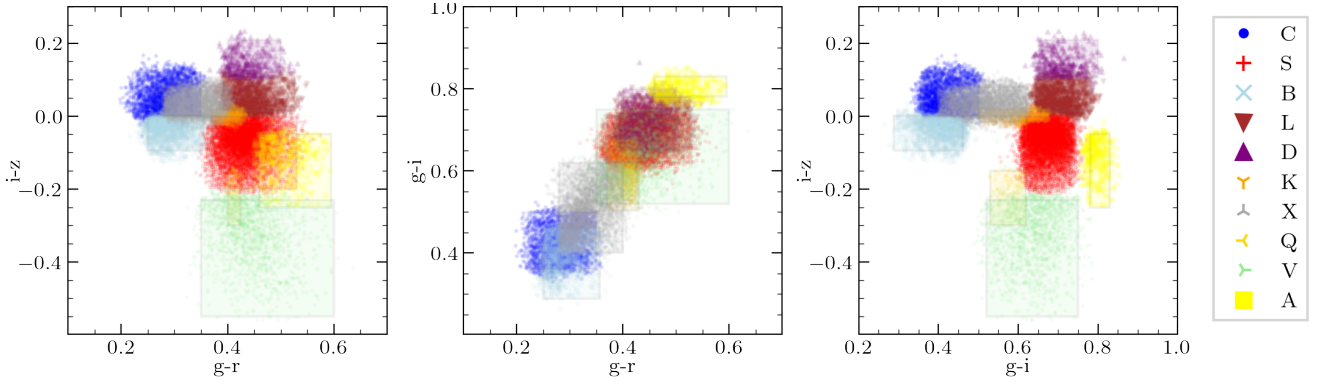


**Fig. 10.** Taxonomy of 29,779 SkyMapper asteroids with a probability larger than 0.2 with three colors. Boxes show the boundaries of the taxonomic classes. Color points mark individual asteroids.

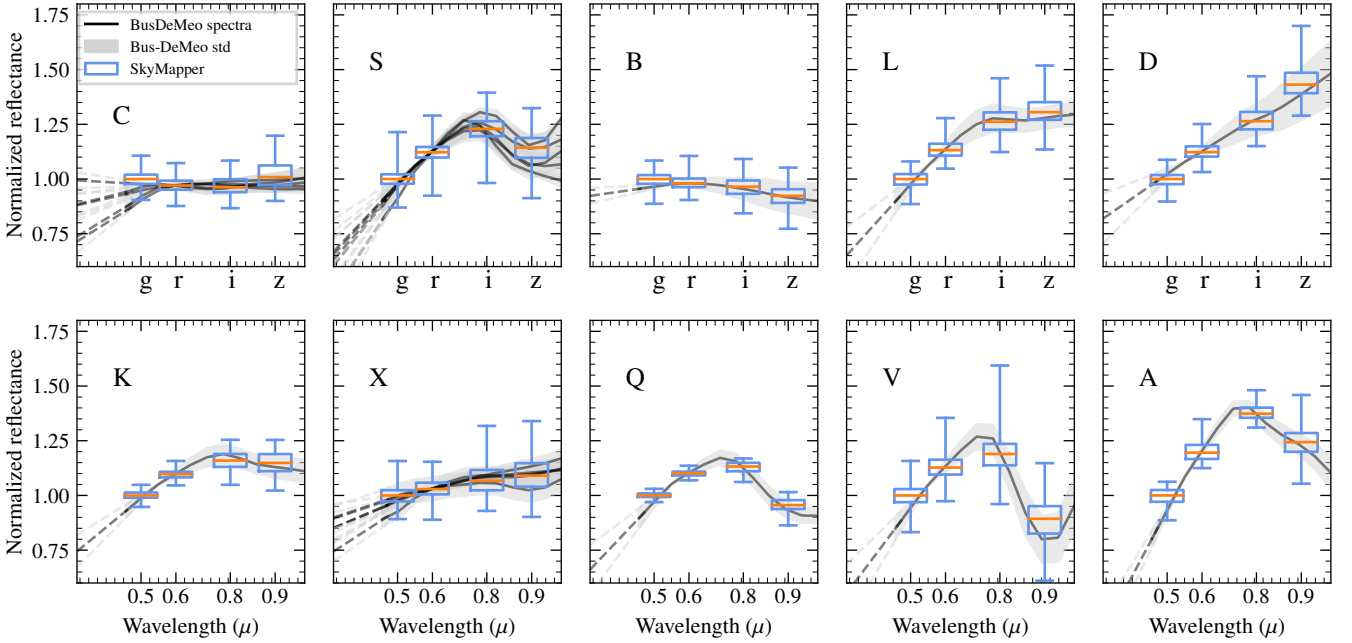


**Fig. 11.** Pseudo-reflectance spectra of asteroids based on their  $g-r$ ,  $g-i$ , and  $i-z$  colors. We indicate the average wavelength of each filter in the lower plots. The distribution of values for each band is represented by whiskers (95% extrema, and the 25, 50, and 75% quartiles). For each class, we also represent the associated template spectra of the Bus-DeMeo taxonomy (DeMeo et al. 2009).

It is interesting to note that even such a simplistic taxonomy criterion provides a very good agreement with spectral observations (Figure 16).

## 8. Future Work

The present catalog represents the first release of SSOs observed by the SkyMapper Southern Survey, based on the data from its third data release (DR3). These data extend the multi-filter photometry provided by the SDSS, which finished its imaging survey in 2009 (although still used by the community, see Sergeev & Carry 2021; Beck & Poch 2021, for instance). SkyMapper is still operating and we plan to release observations of SSOs in upcoming data releases. SkyMapper near-simultaneous acquisition of different filters provides instantaneous determination of colors, which can be used by the community even with the start of operations of the upcoming Legacy Survey of Space and Time (LSST) by the Vera C. Rubin observatory that will require

years to build the phase functions needed to determine SSO colors (Jones et al. 2009; Mahlke et al. 2021).

SkyMapper multi-filter observations are rather unique as of today. The observatories that submitted most data to the Minor Planet Center so far this year (2021) are Catalina Sky Survey, ATLAS (Asteroid Terrestrial-impact Last Alert System), and Pan-STARRS. While Catalina observed the most, it has a wide optical filter only. ATLAS uses two filters and its observing cadence allows for phase functions to be constructed (Mahlke et al. 2021), and a single color can be used for rough taxonomic classification (see Subsection 7.3 and Erasmus et al. 2020). Pan-STARRS has lately contributed to most NEA discoveries, but has relied on  $g$ ,  $r$ ,  $i$  and a wide  $w$  filters, precluding spectral classification as the  $z$  filter probes the  $1\mu\text{m}$  band (the most characteristic spectral feature in all major taxonomies since Chapman et al. (1975)).

Finally, considering the limiting magnitude of SkyMapper, it is unlikely that a large number of unknown SSOs may be dis-

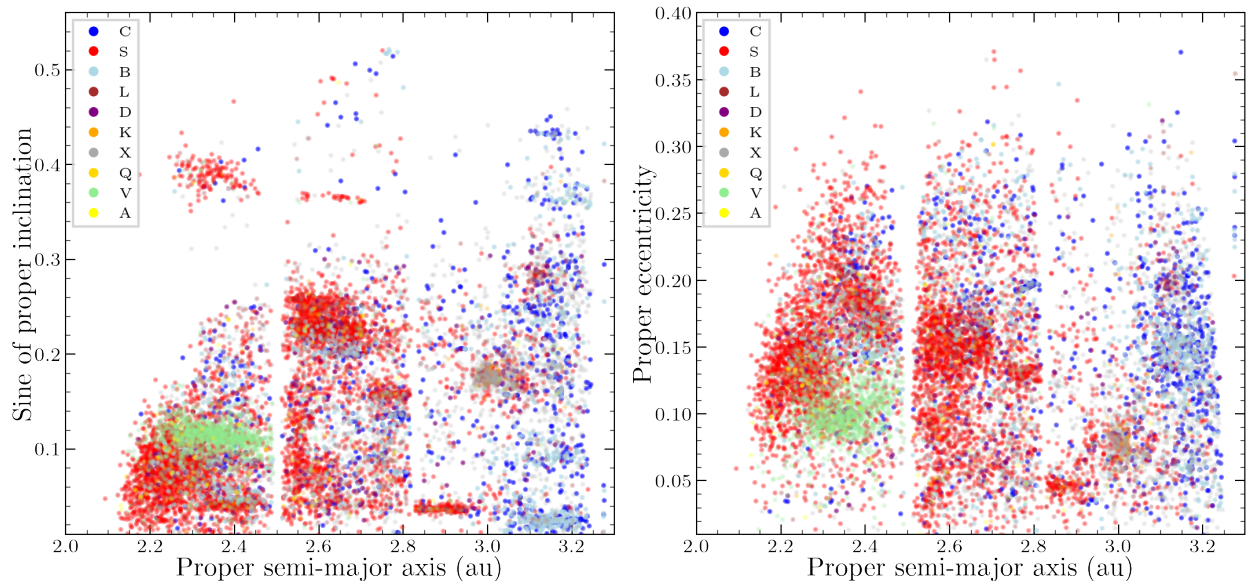


**Fig. 12.** Orbital distribution of the SSOs, color-coded by taxonomic class based on their  $g - r$ ,  $g - i$ , and  $i - z$  colors.

Other sources	A	38	0	0	0	0	0	3	0	0	
	B	0	47	27	1	0	0	0	1	0	5
	C	0	26	18	3	0	2	0	0	0	9
	D	0	0	0	30	0	4	0	0	0	0
	K	0	1	1	6	24	8	0	3	0	4
	L	6	1	1	26	14	44	0	4	1	1
	Q	0	0	0	0	0	0	0	0	1	0
	S	56	1	1	11	29	21	25	83	8	1
	V	0	1	1	1	0	0	75	1	89	0
	X	0	22	53	21	33	21	0	3	0	80
		A	B	C	D	K	L	Q	S	V	X
		SkyMapper									

**Fig. 13.** Confusion matrix of the taxonomy of 1,697 obtained by spectra asteroids and from SkyMapper observations based on their  $g - r$ ,  $g - i$ , and  $i - z$  colors. The values are reported in percent.

covered in its images, and we plan to proceed with the extraction of known SSOs only in future releases.

## 9. Conclusion

We extracted known Solar System objects from SkyMapper Southern Survey DR3 images. We applied a suite of filters to minimize contamination. We release a catalog of 880,528 individual observations, consisting of 205,515 unique, known SSOs. The catalog contains the SkyMapper identification, astrometry,

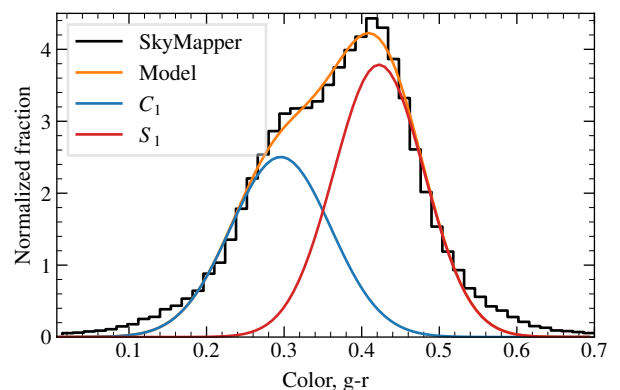


**Fig. 14.** The  $g - r$  color distribution of SkyMapper asteroids (black) where fitted by the sum of two normal distributions (orange) which could be associated with  $C_1$  (opaque-rich, blue) and  $S_1$  (mafic-silicate rich, red) asteroids complexes.

photometry, SSO identification, geometry of observation, and taxonomy. Its content is fully described in [Appendix A](#).

The catalog completeness is estimated to be about 97% down to  $V = 18$  mag and the purity to almost 100% down to  $V = 20$  mag. The present catalog contains photometry of 669 near-Earth asteroids, 2,487 Mars-crossers, 196,269 main-belt asteroids, and 1,928 Jupiter trojans.

There are 100,005 asteroids which were already observed by the SDSS ([Sergeyev & Carry 2021](#)). Combined, the SDSS and SkyMapper data sets account almost 80% of all MBAs with an absolute magnitude ( $H$ ) between 10 and 16, each data set contributing equally. As most of the brighter asteroids ( $H < 10$ ) have spectra, the present SkyMapper release represents a major step toward completeness of taxonomic classification of asteroids in the main belt ([Figure 18](#)). The situation is somewhat similar for NEAs and Mars-Crossers, with a completeness above 80% of these two populations down to an absolute magnitude of 16, although spectral surveys contributed more (e.g., [Perna et al. 2018](#); [Devogèle et al. 2019](#); [Binzel et al. 2019](#)). The distant KBOs are



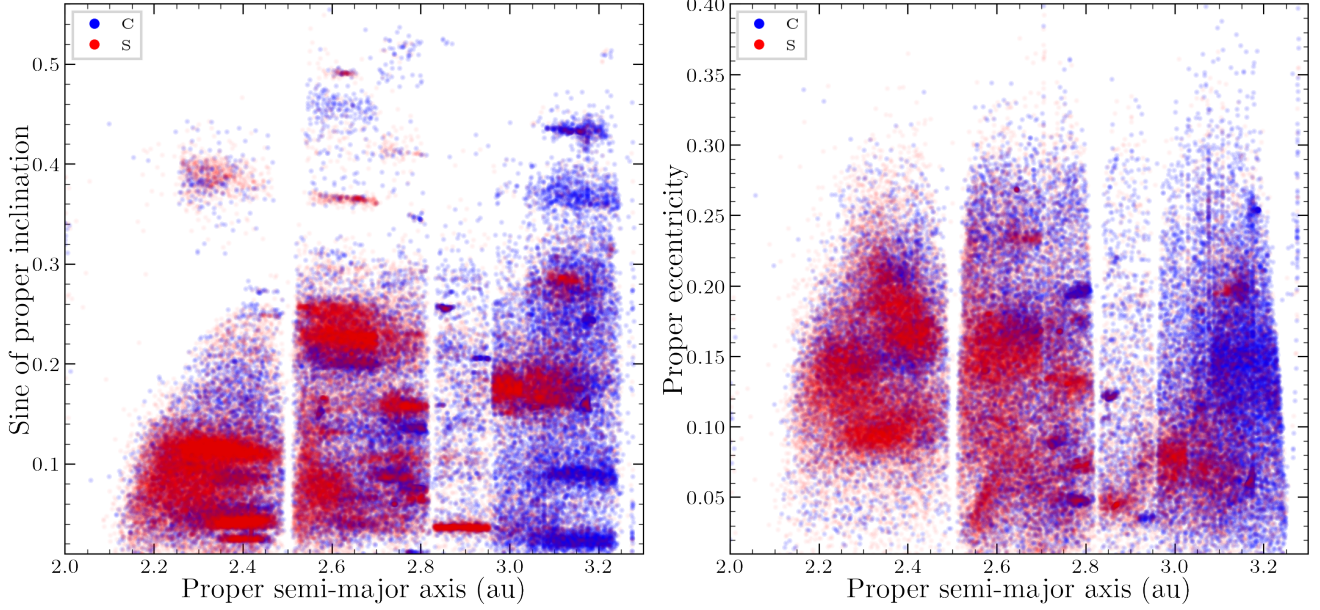


**Fig. 15.** Orbital distribution of the SkyMapper SSOs, color-coded by taxonomic class based on  $g-r$  color only.

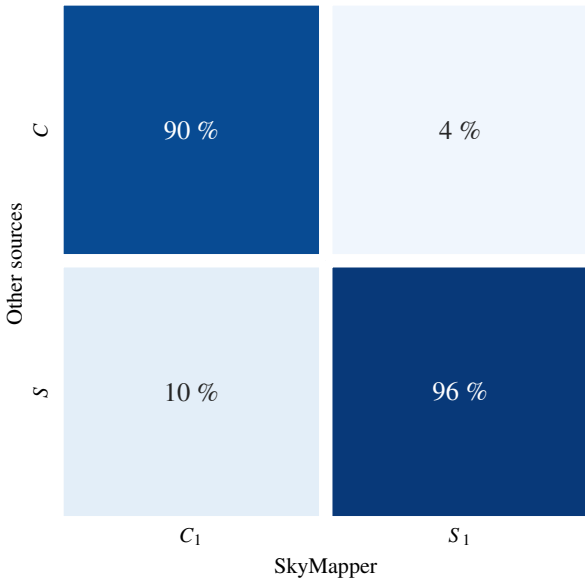


**Fig. 16.** The confusion matrix of C and S taxonomy complexes of 1129 joint asteroids with known by spectra taxonomy and SkyMapper taxonomy based on  $g-r$  colors only.

the population with the lowest completeness of color characterization, below 50% (caveat: we have not attempted to compile spectra of KBOs here). As SkyMapper is an on-going survey, this completeness will increase with future releases.

We compared taxonomy classification of 6,965 common asteroids between the recent SDSS release (Sergeyev & Carry 2021) and the present SkyMapper catalog, considering only SSOs with a taxonomy based on three colors and a probability above 0.2. The confusion matrix presented in Figure 17 shows

SDSS	A	3	1	0	0	3	10	0	32	1	2
	B	1	64	38	0	0	0	0	0	0	11
	C	0	145	137	0	1	0	0	3	0	160
	D	0	0	2	36	10	33	1	29	1	42
	K	0	1	1	0	5	1	0	20	0	19
	L	4	0	0	9	13	53	0	104	2	22
	Q	0	0	0	0	0	0	0	0	1	0
	S	37	13	7	18	72	149	7	1707	104	145
	V	2	1	1	0	0	6	6	67	388	10
	X	0	29	74	1	10	6	0	18	2	359
		A	B	C	D	K	L	Q	S	V	X
		SkyMapper									

**Fig. 17.** The confusion matrix of 6,965 asteroids taxonomy from the SDSS and SkyMapper with the probability accuracy of more than 0.2

a good agreement for the most common complexes like S, C, B, and V. Some confusion is present between less prominent classes, in particular between K/L/A and S. This highlights both the strength and the limitation of taxonomic classification based on broad-band colors only.

*Acknowledgements.* This research has been conducted within the NEOROCKS project, which has received funding from the European Union's Horizon 2020 research and innovation programme under grant agreement No 870403. CAO was supported by the Australian Research Council (ARC) through Discovery Project DP190100252. SWC acknowledges support from the National Research Foundation of Korea (NRF) grant, No.2020R1A2C3011091, funded by the Ko-

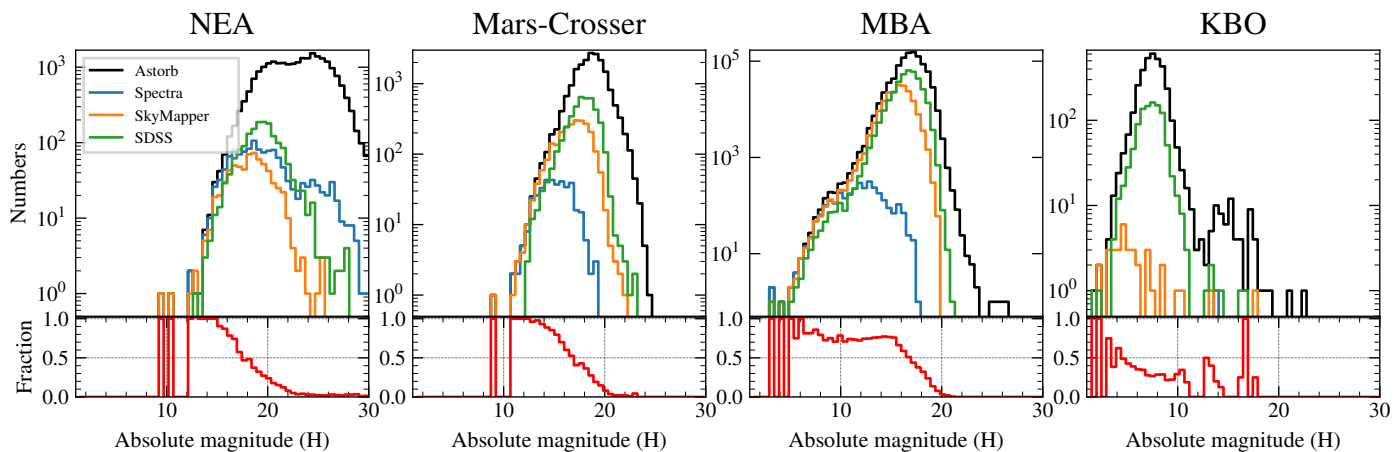


**Fig. 18.** Comparison of the number of SSOs with either spectra, SDSS colors, or SkyMapper colors, compared with the total number of SSO (taken from Astorb) for each of the NEA, Mars-Crossers, MBA, and KBO dynamical populations.

rea government (MSIT).

We thank J. Berthier, F. Spoto, M. Mählke for discussions related to the present article.

The national facility capability for SkyMapper has been funded through ARC LIEF grant LE130100104 from the Australian Research Council, awarded to the University of Sydney, the Australian National University, Swinburne University of Technology, the University of Queensland, the University of Western Australia, the University of Melbourne, Curtin University of Technology, Monash University and the Australian Astronomical Observatory. SkyMapper is owned and operated by The Australian National University's Research School of Astronomy and Astrophysics. The survey data were processed and provided by the SkyMapper Team at ANU. The SkyMapper node of the All-Sky Virtual Observatory (ASVO) is hosted at the National Computational Infrastructure (NCI). Development and support of the SkyMapper node of the ASVO has been funded in part by Astronomy Australia Limited (AAL) and the Australian Government through the Commonwealth's Education Investment Fund (EIF) and National Collaborative Research Infrastructure Strategy (NCRIS), particularly the National eResearch Collaboration Tools and Resources (NeCTAR) and the Australian National Data Service Projects (ANDS).

The Pan-STARRS1 Surveys (PS1) and the PS1 public science archive have been made possible through contributions by the Institute for Astronomy, the University of Hawaii, the Pan-STARRS Project Office, the Max-Planck Society and its participating institutes, the Max Planck Institute for Astronomy, Heidelberg and the Max Planck Institute for Extraterrestrial Physics, Garching, The Johns Hopkins University, Durham University, the University of Edinburgh, the Queen's University Belfast, the Harvard-Smithsonian Center for Astrophysics, the Las Cumbres Observatory Global Telescope Network Incorporated, the National Central University of Taiwan, the Space Telescope Science Institute, the National Aeronautics and Space Administration under Grant No. NNX08AR22G issued through the Planetary Science Division of the NASA Science Mission Directorate, the National Science Foundation Grant No. AST-1238877, the University of Maryland, Eotvos Lorand University (ELTE), the Los Alamos National Laboratory, and the Gordon and Betty Moore Foundation.

This research made use of the cross-match service provided by CDS, Strasbourg (Pineau et al. 2017), the IMCCE's SkyBoT and Skybot3D VO tools (Berthier et al. 2006, 2016), the JPL Horizons system (Giorgini et al. 1996), the SVO Filter Profile Service (<http://svo2.cab.inta-csic.es/theory/fps/>) supported from the Spanish MINECO through grant AYA2017-84089 (Rodrigo et al. 2012), and TOPCAT/STILTS (Taylor 2005). Thanks to the developers.

## References

- Beck, P. & Poch, O. 2021, *Icarus*, 365, 114494
- Berthier, J., Carry, B., Vachier, F., Eggl, S., & Santerne, A. 2016, *MNRAS*, 458, 3394
- Berthier, J., Vachier, F., Thuillot, W., et al. 2006, in *Astronomical Society of the Pacific Conference Series*, Vol. 351, *Astronomical Data Analysis Software and Systems XV*, ed. C. Gabriel, C. Arviset, D. Ponz, & S. Enrique, 367
- Binzel, R. P., DeMeo, F. E., Turtelboom, E. V., et al. 2019, *Icarus*, 324, 41
- Brown, A. G. A., Vallenari, A., Prusti, T., et al. 2018, *A&A*, 616, A1
- Bus, S. J. & Binzel, R. P. 2002, *Icarus*, 158, 146
- Carry, B. 2018, *A&A*, 609, A113
- Carvano, J. M., Hasselmann, P. H., Lazzaro, D., & Mothé-Diniz, T. 2010, *A&A*, 510, A43
- Casagrande, L., Wolf, C., Mackey, A. D., et al. 2019, *MNRAS*, 482, 2770
- Chambers, K. C., Magnier, E. A., Metcalfe, N., et al. 2016, *arXiv e-prints*, arXiv:1612.05560
- Chapman, C. R., Morrison, D., & Zellner, B. H. 1975, *Icarus*, 25, 104
- Clement, M. S., Morbidelli, A., Raymond, S. N., & Kaib, N. A. 2020, *MNRAS*, 492, L56
- DeMeo, F., Binzel, R. P., Carry, B., Polishook, D., & Moskovitz, N. A. 2014, *Icarus*, 229, 392
- DeMeo, F., Binzel, R. P., Slivan, S. M., & Bus, S. J. 2009, *Icarus*, 202, 160
- DeMeo, F. & Carry, B. 2014, *Nature*, 505, 629
- DeMeo, F. E. & Carry, B. 2013, *Icarus*, 226, 723
- DeMeo, F. E., Polishook, D., Carry, B., et al. 2019, *Icarus*, 322, 13
- Devogèle, M., Moskovitz, N., Thirouin, A., et al. 2019, *AJ*, 158, 196
- Erasmus, N., Navarro-Meza, S., McNeill, A., et al. 2020, *ApJS*, 247, 13
- Fornasier, S., Dotto, E., Marzari, F., et al. 2004, *Icarus*, 172, 221
- Fornasier, S., Lantz, C., Barucci, M. A., & Lazzarin, M. 2014, *Icarus*, 233, 163
- Giorgini, J. D., Yeomans, D. K., Chamberlin, A. B., et al. 1996, in *AAS/Division for Planetary Sciences Meeting Abstracts*, Vol. 28, *AAS/Division for Planetary Sciences Meeting Abstracts #28*, 25.04
- Graves, K., Minton, D., Hirabayashi, M., DeMeo, F., & Carry, B. 2018, *Icarus*, 304, 162
- Holmberg, J., Flynn, C., & Portinari, L. 2006, *MNRAS*, 367, 449
- Huang, Y., Chen, B. Q., Yuan, H. B., et al. 2019, *ApJS*, 243, 7
- Ivezić, Ž., Tabachnik, S., Rafikov, R., et al. 2001, *AJ*, 122, 2749
- Jenniskens, P., Gabadadze, M., Yin, Q.-Z., et al. 2021, *Meteoritics & Planetary Science*, 56, 844
- Jones, R. L., Chesley, S. R., Connolly, A. J., et al. 2009, *Earth Moon and Planets*, 105, 101
- Lazzaro, D., Angeli, C. A., Carvano, J. M., et al. 2004, *Icarus*, 172, 179
- Levison, H. F., Bottke, W. F., Gounelle, M., et al. 2009, *Nature*, 460, 364
- Mählke, M., Carry, B., & Denneau, L. 2021, *Icarus*, 354, 114094
- Morbidelli, A., Walsh, K. J., O'Brien, D. P., Minton, D. A., & Bottke, W. F. 2015, *The Dynamical Evolution of the Asteroid Belt*, 493–507
- Nesvorný, D., Jedicke, R., Whiteley, R. J., & Ivezić, Ž. 2005, *Icarus*, 173, 132
- Oke, J. B. & Gunn, J. E. 1983, *ApJ*, 266, 713
- Onken, C. A., Wolf, C., Bessell, M. S., et al. 2019, *PASA*, 36, e033
- Parker, A., Ivezić, Ž., Jurić, M., et al. 2008, *Icarus*, 198, 138
- Perna, D., Barucci, M. A., Fulchignoni, M., et al. 2018, *Planet. Space Sci.*, 157, 82
- Pickles, A. J. 1998, *PASP*, 110, 863
- Pineau, F. X., Derriere, S., Motch, C., et al. 2017, *A&A*, 597, A89
- Popescu, M., Licandro, J., Morate, D., et al. 2016, *A&A*, 591, A115
- Rodrigo, C., Solano, E., Bayo, A., & Rodrigo, C. 2012, *SVO Filter Profile Service Version 1.0*, Tech. rep.
- Sergeyev, A. V. & Carry, B. 2021, *A&A*, 652, A59
- Siegel, A. F. 1982, *Biometrika*, 69, 242
- Szabó, G. M., Ivezić, Ž., Jurić, M., Lupton, R., & Kiss, L. L. 2004, *MNRAS*, 348, 987
- Taylor, M. B. 2005, in *Astronomical Society of the Pacific Conference Series*, Vol. 347, *Astronomical Data Analysis Software and Systems XIV*, ed. P. Shopbell, M. Britton, & R. Ebert, 29
- Tholen, D. J. 1989, in *Asteroids II*, ed. R. P. Binzel, T. Gehrels, & M. S. Matthews, 1139–1150
- Wolf, C., Onken, C. A., Luvaul, L. C., et al. 2018, *PASA*, 35, e010

## Appendix A: Description of catalogs

We describe here the three catalogs of Solar System objects (SSOs) we release. The detection catalog (Table A.1) contains all the information on each observation. (mid-observing time, coordinates, etc.). The color catalogs contains all the measured SSO colors (Table A.2), while the object catalog (Table A.3) contains a single entry per SSOs, with its average colors.

The Table A.4 contains estimated taxonomy and orbital elements of asteroids. The most probably taxonomy depends of the color priority in the follow sequence:  $g-r$ ,  $g-i$ ,  $i-z$  colors have the first priority, two colors  $g-r$ ,  $i-z$ ,  $g-i$ ,  $i-z$ ,  $r-i$ ,  $i-z$  have a priority 2, 3, 4 consequently and  $g-r$  color priority 5.

**Table A.1.** Description of the SkyMapper catalog of SSO observations.

ID	Name	Unit	Description
1	source		Source unique identifier
2	frame		Image unique identifier
3	JD	day	Julian Date of observation
4	filter		Filter name ( $u, v, g, r, i, z$ )
5	exptime	s	Exposure time
6	ra	deg	J2000 Right Ascension
7	dec	deg	J2000 Declination
8	psfMag	mag	PSF magnitude
9	psfMagErr	mag	PSF magnitude uncertainty
10	petroMag	mag	Petrosian magnitude
11	petroMagErr	mag	Petrosian magnitude uncertainty
12	number		SSO IAU number
13	name		SSO IAU designation
14	dynclass		SSO dynamical class
15	ra_rate	"/h	RAcos(DEC) rate of motion
16	dec_rate	"/h	DEC rate
17	V	mag	Predicted visual magnitude

**Table A.2.** Description of the color catalog extracted from all SkyMapper SSOs observations.

ID	Name	Unit	Description
1	number		SSO IAU number
2	name		SSO IAU designation
3	JD	day	Average epoch of observation
4	color		Name of color (e.g., $g-r$ )
5	dmag	mag	Value of the color
6	edmag	mag	Uncertainty on the color
7	dmjd	day	Delay between filters

**Table A.3.** Description of the catalog of measured weighted mean SSOs colors.

ID	Name	Unit	Description
1	number		SSO IAU number
2	name		SSO IAU designation
4	color		Name of color (e.g., $g-r$ )
5	wdmag	mag	Weighted value of the color
6	var	mag	Weighted uncertainty of the color measurements
7	n		Number of color measurements, 0 - computed
6	emag	mag	Mean value of the color uncertainties
7	dmjd	day	Mean time difference between color measurements

**Table A.4.** Description of individual SkyMapper SSOs color catalog (measured and computed) and their taxonomy.

ID	Name	Unit	Description
1	number		SSO IAU number
2	name		SSO IAU designation
3	dynclass		SSO dynamic class
4-18	m[*color list]	mag	set of the color magnitude values
29-43	e[*color list]	mag	set of the color uncertainties
44-58	d[*color list]	day	set of time values between observations
59-69	p[C, S, B, L, D, K, X, Q, V, A, U]		probability of the complex values
70	complex		Most probably complex
71	pcomplex		Probability value of the complex
72	complex1		First the most probably complex
73	complex2		Second the most probably complex
74	pcomplex1		Probability value of first the most probably complex
75	pcomplex2		Probability value of second the most probably complex
76	nc		Number of colors where used for the taxonomy estimation

\* color list:  $u-v, u-g, u-r, u-i, u-z, v-g, v-r, v-i, v-z, g-r, g-i, i-z, g-z, r-i, r-z$

## Appendix B: Multi-color taxonomy

We present here the color distribution, pseudo-reflectance, confusion matrix, orbital distribution and taxonomy boundaries of asteroids with two colors.

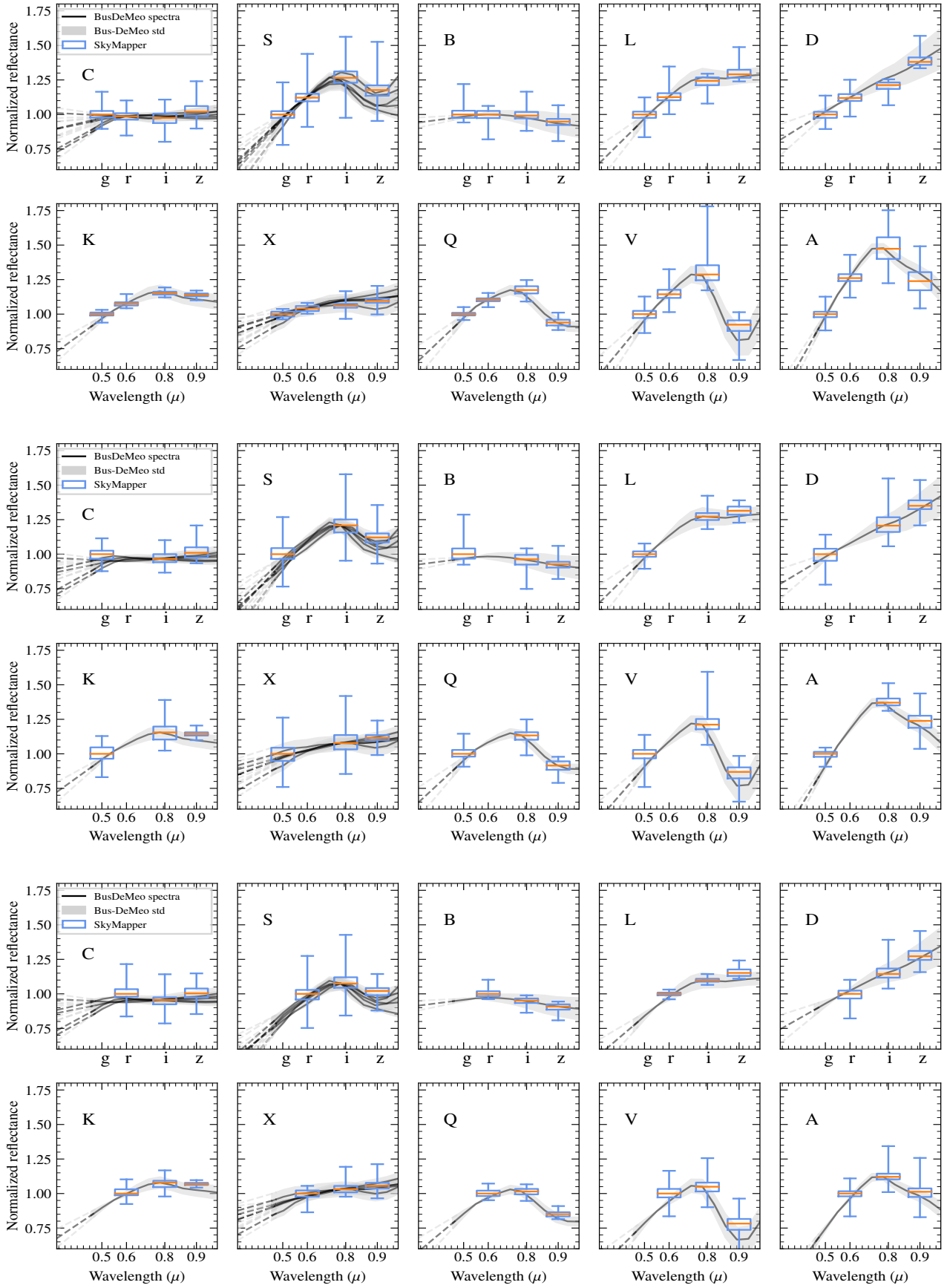
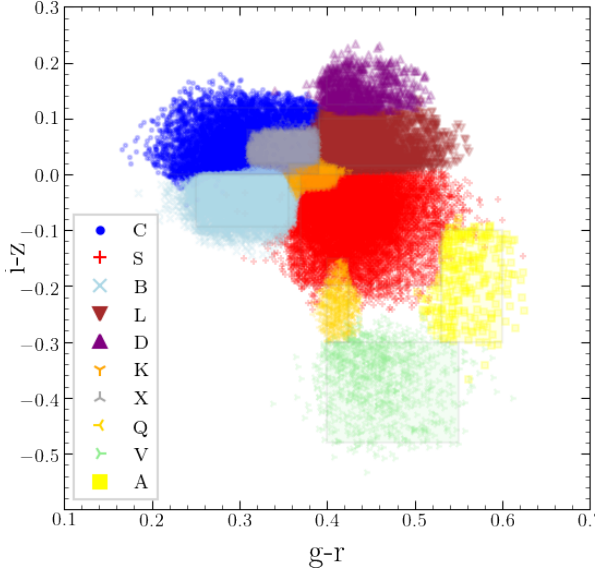
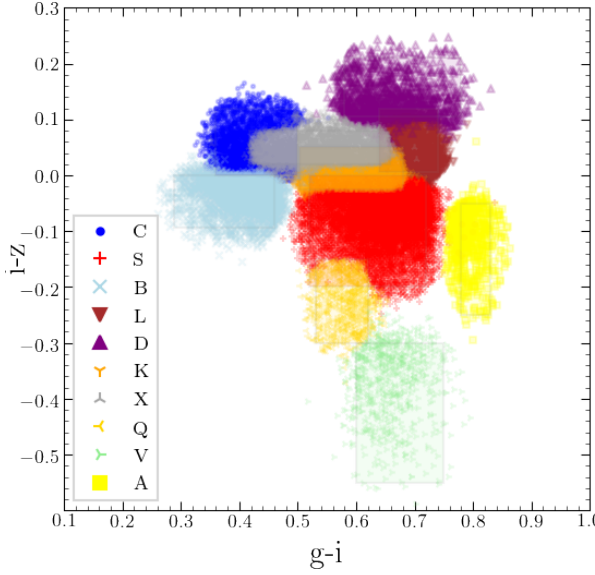


**Fig. B.1.** Grouped by taxonomic class pseudo-reflectance spectra of asteroids based on two color taxonomy (top:  $g-r$ ,  $i-z$  colors), (middle:  $g-i$ ,  $i-z$  colors) and (bottom:  $r-i$ ,  $i-z$  colors). We indicate the average wavelength of each filter in the lower plots. The distribution of values for each band is represented by whiskers (95% extrema, and the 25, 50, and 75% quartiles). For each, we also represent the associated template spectra of the Bus-DeMeo taxonomy (DeMeo et al. 2009).



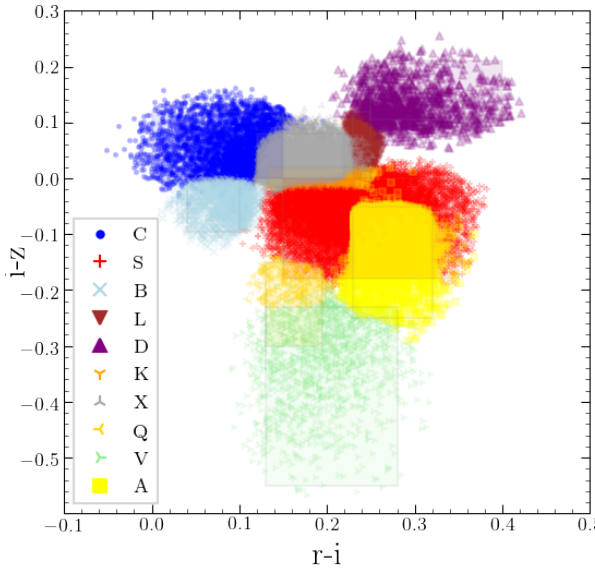
Other sources	A	4	0	0	0	0	0	0	3	0
B	0	47	33	4	6	0	0	4	0	11
C	0	45	50	25	3	8	0	1	0	38
D	0	0	0	21	0	4	0	0	0	0
K	4	1	1	7	34	8	0	2	0	6
L	14	1	1	20	12	57	0	6	1	3
Q	0	0	0	0	0	0	40	0	8	0
S	79	4	2	9	34	20	60	86	14	3
V	0	0	0	0	0	0	0	0	73	0
X	0	1	12	13	9	4	0	1	0	39
	A	B	C	D	K	L	Q	S	V	X

SkyMapper, (g-r vs. i-z)



Other sources	A	26	0	0	0	0	0	4	2	0
B	0	52	31	1	0	0	14	1	0	5
C	0	30	28	0	0	0	0	0	0	15
D	4	0	2	49	0	11	0	1	0	1
K	0	1	3	9	43	11	0	8	0	13
L	9	0	0	14	4	44	0	3	2	1
Q	0	1	0	0	0	0	43	1	17	0
S	57	7	4	9	39	13	29	79	8	4
V	0	0	1	1	0	0	14	0	71	0
X	4	8	31	18	14	20	0	3	0	61
	A	B	C	D	K	L	Q	S	V	X

SkyMapper, (g-i vs. i-z)



Other sources	A	39	2	1	1	9	6	11	33	1	1
B	0	25	7	1	0	0	11	1	0	0	1
C	0	23	16	2	0	3	0	1	0	0	9
D	0	0	1	51	3	6	0	0	0	0	1
K	0	2	11	8	18	8	0	3	0	0	6
L	0	2	0	15	12	36	0	1	0	0	5
Q	0	0	0	0	0	0	22	0	7	0	0
S	52	18	14	9	42	17	22	55	5	9	0
V	0	1	0	0	0	0	33	1	85	0	0
X	10	25	49	13	15	25	0	4	1	0	69
	A	B	C	D	K	L	Q	S	V	X	

SkyMapper, (r-i vs. i-z)

**Fig. B.2.** Taxonomy of SkyMapper asteroids with a probability value more than 0.2 with two (top:  $g-r$ ,  $i-z$ , middle:  $g-i$ ,  $i-z$  and bottom:  $r-i$ ,  $i-z$ ) colors. Boxes show the boundaries of the taxonomic classes. Color points mark an individual asteroids.

**Fig. B.3.** Confusion matrices of asteroids taxonomy based on (top:  $g-r$ ,  $i-z$ , middle:  $g-i$ ,  $i-z$  and bottom:  $r-i$ ,  $i-z$ ) SkyMapper colors opposite taxonomy from published spectral observations. The values are reported in percents.

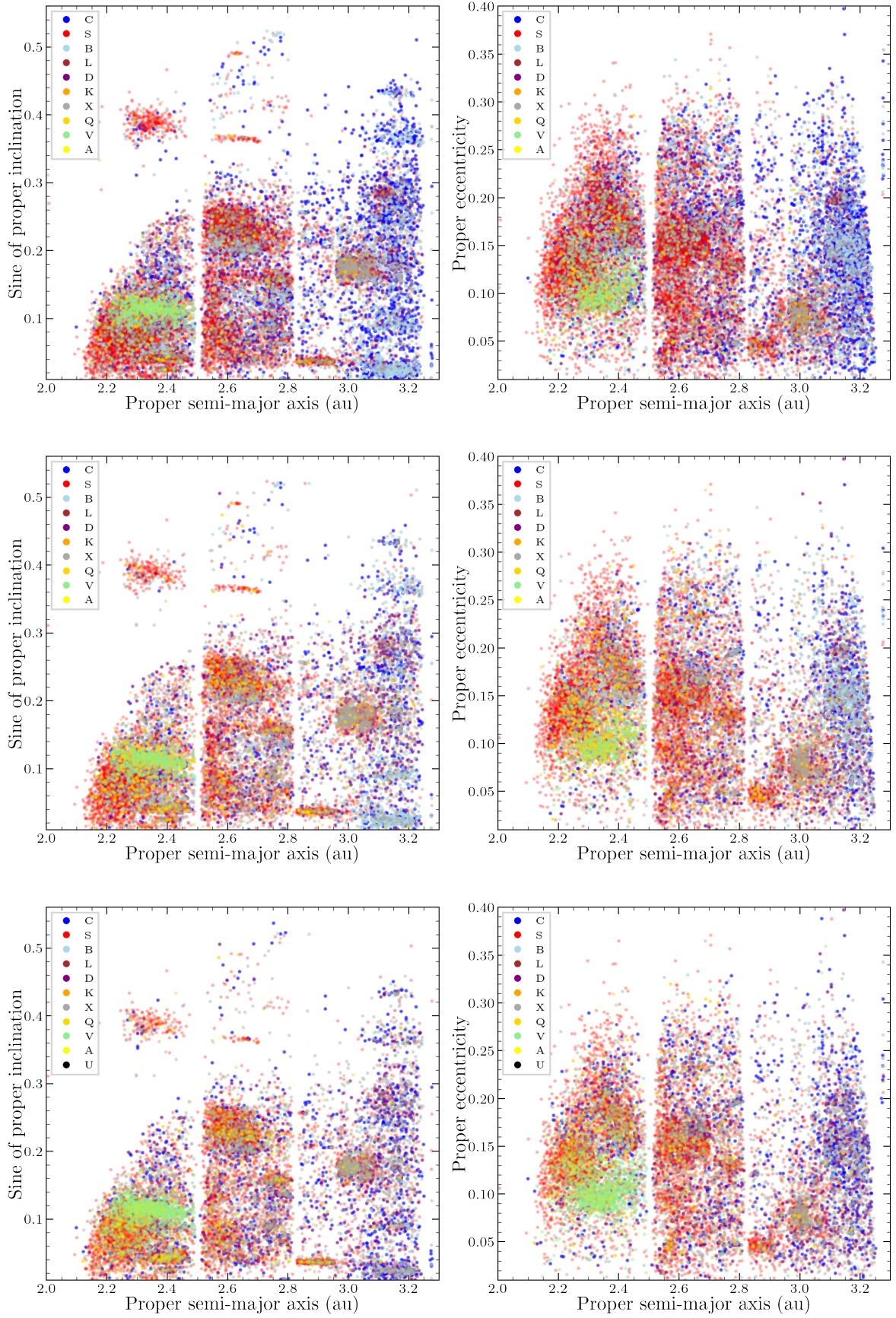


**Fig. B.4.** Orbital distribution of the SkyMapper SSOs, color-coded by taxonomic class based on their (top:  $g-r, i-z$ , middle:  $g-i, i-z$  and bottom:  $r-i, i-z$ ) colors

**Table B.1.** Boundaries of taxonomy complexes in g-r, g-i, i-z color space.

complex	$gr_{min}$	$gr_{max}$	$iz_{min}$	$iz_{max}$	$gi_{min}$	$gi_{max}$
C	0.220	0.350	0.000	0.120	0.360	0.50
S	0.370	0.530	-0.200	0.000	0.620	0.73
B	0.250	0.356	-0.094	0.001	0.288	0.46
L	0.391	0.527	0.015	0.120	0.650	0.78
D	0.400	0.500	0.105	0.210	0.650	0.80
K	0.370	0.430	-0.015	0.020	0.503	0.68
X	0.280	0.400	0.000	0.080	0.400	0.62
Q	0.400	0.425	-0.300	-0.150	0.530	0.62
V	0.350	0.600	-0.550	-0.230	0.520	0.75
A	0.459	0.595	-0.250	-0.050	0.780	0.83

**Table B.2.** Boundaries of taxonomy complexes in g-r, i-z color space.

complex	$gr_{min}$	$gr_{max}$	$iz_{min}$	$iz_{max}$
C	0.220	0.391	0.000	0.120
S	0.370	0.530	-0.200	0.000
B	0.250	0.356	-0.094	0.001
L	0.391	0.527	0.015	0.100
D	0.400	0.500	0.125	0.190
K	0.356	0.411	-0.025	0.020
X	0.309	0.391	0.020	0.080
Q	0.400	0.425	-0.300	-0.150
V	0.400	0.550	-0.480	-0.300
A	0.530	0.600	-0.300	-0.100

**Table B.3.** Boundaries of taxonomy complexes in g-i, i-z color space.

complex	$gi_{min}$	$gi_{max}$	$iz_{min}$	$iz_{max}$
C	0.360	0.500	0.000	0.120
S	0.520	0.720	-0.200	0.000
B	0.288	0.460	-0.094	0.001
L	0.640	0.740	0.005	0.120
D	0.580	0.780	0.105	0.210
K	0.503	0.680	-0.025	0.050
X	0.417	0.658	0.020	0.080
Q	0.530	0.620	-0.300	-0.150
V	0.600	0.750	-0.550	-0.300
A	0.780	0.830	-0.250	-0.050

**Table B.4.** Boundaries of taxonomy complexes in r-i, i-z color space.

complex	$ri_{min}$	$ri_{max}$	$iz_{min}$	$iz_{max}$
C	0.000	0.150	0.000	0.120
S	0.150	0.350	-0.180	0.000
B	0.040	0.100	-0.095	0.001
L	0.230	0.250	0.000	0.120
D	0.250	0.400	0.105	0.210
K	0.133	0.250	-0.015	0.020
X	0.120	0.220	0.000	0.080
Q	0.130	0.195	-0.300	-0.150
V	0.130	0.280	-0.550	-0.230
A	0.230	0.320	-0.250	-0.050